

HFSB-seeding for large-scale tomographic PIV in wind tunnels

Caridi, Giuseppe Carlo Alp; Ragni, Daniele; Sciacchitano, Andrea; Scarano, Fulvio

DOI

[10.1007/s00348-016-2277-7](https://doi.org/10.1007/s00348-016-2277-7)

Publication date

2016

Document Version

Final published version

Published in

Experiments in Fluids: experimental methods and their applications to fluid flow

Citation (APA)

Caridi, G. C. A., Ragni, D., Sciacchitano, A., & Scarano, F. (2016). HFSB-seeding for large-scale tomographic PIV in wind tunnels. *Experiments in Fluids: experimental methods and their applications to fluid flow*, 57(12), Article 190. <https://doi.org/10.1007/s00348-016-2277-7>

Important note

To cite this publication, please use the final published version (if applicable). Please check the document version above.

Copyright

Other than for strictly personal use, it is not permitted to download, forward or distribute the text or part of it, without the consent of the author(s) and/or copyright holder(s), unless the work is under an open content license such as Creative Commons.

Takedown policy

Please contact us and provide details if you believe this document breaches copyrights. We will remove access to the work immediately and investigate your claim.

HFSB-seeding for large-scale tomographic PIV in wind tunnels

Giuseppe Carlo Alp Caridi¹ · Daniele Ragni¹ · Andrea Sciacchitano¹ · Fulvio Scarano¹

Received: 26 April 2016 / Revised: 27 October 2016 / Accepted: 8 November 2016 / Published online: 19 November 2016
© The Author(s) 2016. This article is published with open access at Springerlink.com

Abstract A new system for large-scale tomographic particle image velocimetry in low-speed wind tunnels is presented. The system relies upon the use of sub-millimetre helium-filled soap bubbles as flow tracers, which scatter light with intensity several orders of magnitude higher than micron-sized droplets. With respect to a single bubble generator, the system increases the rate of bubbles emission by means of transient accumulation and rapid release. The governing parameters of the system are identified and discussed, namely the bubbles production rate, the accumulation and release times, the size of the bubble injector and its location with respect to the wind tunnel contraction. The relations between the above parameters, the resulting spatial concentration of tracers and measurement of dynamic spatial range are obtained and discussed. Large-scale experiments are carried out in a large low-speed wind tunnel with $2.85 \times 2.85 \text{ m}^2$ test section, where a vertical axis wind turbine of 1 m diameter is operated. Time-resolved tomographic PIV measurements are taken over a measurement volume of $40 \times 20 \times 15 \text{ cm}^3$, allowing the quantitative analysis of the tip-vortex structure and dynamical evolution.

1 Introduction

Tomographic PIV has been employed in a wide range of applications since its introduction in 2006 (Elsinga et al. 2006). One of the recognized limitations of this technique is the extent of the measurement volume, limited to a typical size of a few hundreds of cubic centimetres (Scarano 2013), especially in airflow experiments with micron-sized particle tracers. This limitation has hindered the use of tomographic PIV for applications of industrial aerodynamics, where the region of interest may attain the order of a metre. The main factor precluding the upscaling of the technique is the limited laser pulse energy when distributed over a large volume, combined with a small optical aperture to ensure in-focus imaging conditions. As a result, the amount of light collected by the cameras for each particle decreases when increasing the size of the measurement domain. The use of larger tracer particles as a means to increase the scattered intensity has been demonstrated to affect the tracing fidelity, which rapidly degrades due to the increase in the particle inertia (Melling 1997). The neutral buoyancy condition reached with sub-millimetre helium-filled soap bubbles (HFSB) tracers has been recently shown to combine the higher scattered intensity with good tracing fidelity. With a time response in the range of 10–30 μs , these tracers are deemed suitable for quantitative studies in low-speed aerodynamics (Scarano et al. 2015).

The use of HFSB as flow tracers dates back to the visualization of several aerodynamic flows, including the flow around a parachute (Pounder 1956; Klimas 1973), the separated flow around an airfoil (Hale et al. 1971a), wing-tip vortices (Hale et al. 1971b; Babie and Nelson 2010) and jet flows (Ferrell et al. 1985). HFSB tracers have been mostly used to visualize individual path-lines within complex flows. However, the low production rate of 10^3 – 10^4 bubbles

Electronic supplementary material The online version of this article (doi:10.1007/s00348-016-2277-7) contains supplementary material, which is available to authorized users.

✉ Giuseppe Carlo Alp Caridi
G.Caridi@tudelft.nl

¹ Department of Aerospace Engineering, TU Delft, Delft, The Netherlands

per second (Okuno et al. 1993; Müller et al. 2001; <http://www.sageaction.com/>) only allows low seeding concentrations, which makes the image analysis via standard cross-correlation-based approaches unsuited. Moreover, uniform tracer dispersion in the airflow cannot be achieved with the use of a single-point source of tracers.

In a previous work from the authors (Scarano et al. 2015), a system was proposed based on a single bubble generator with production rate of approximately 50,000 bubbles per second coupled with a piston–cylinder system. A larger amount of tracers was injected in the settling chamber of a small wind tunnel allowing time-resolved tomographic PIV measurements over a domain of approximately $20 \times 20 \times 10 \text{ cm}^3$.

A number of questions remains open, namely the achievable spatial resolution and spatial dynamic range of large-scale experiments realized with HFSB as flow tracers. The applicability of these systems in large-scale wind tunnels (with test section of 10 m^2 or larger) has also to be assessed before tomographic PIV can become a viable tool for aerodynamic research at industrial scale.

The present study is structured in two parts. First, the governing parameters of a large-scale seeding system are identified. The relationship between HFSB production rate, spatial concentration and dynamic spatial range (DSR) achievable in the wind tunnel environment is discussed on a theoretical basis. Then, a description of the salient technical aspects of the seeding system is given, which compares the theoretical and the measured increase in bubble concentration with respect to stationary bubble emission. Finally, the technique is applied to study the dynamical evolution of the three-dimensional flow developing from the rotor blade tip of a vertical axis wind turbine (VAWT) of 1 m diameter and 1 m height. The measurements are taken at a rate of 1000 Hz in a volume of $40 \times 20 \times 15 \text{ cm}^3$, which allows following the blade passage and the associated tip-vortex formation, release and spatio-temporal evolution in the inner rotor region. The results obtained with tomographic PIV cross-correlation analysis are compared with the Tomo-PTV approach that follows the VIC+ method (Schneiders and Scarano 2016) in relation to the tip-vortex peak vorticity. The method was successfully applied in the case of a turbulent boundary layer measurement by Schneiders et al. (2016).

2 Spatial resolution and dynamic range

In this section, the relationship between the production rate of the HFSB and the DSR achievable in tomographic PIV measurements is discussed. Moreover, the influence of the location where the tracers are injected, namely upstream or downstream the wind tunnel contraction, is considered.

Following the approach of Adrian (1997), the dynamic spatial range is defined as the ratio between the largest and the smallest resolvable spatial wavelength. Westerweel et al. (2013) have defined the dynamic spatial range as the ratio between the length of the field of view L and the particle tracer displacement Δx namely:

$$\text{DSR} = \frac{L}{\Delta x} \quad (1)$$

Further studies on the spatial resolution of PIV (Raffel et al. 2007; Astarita 2009; Kähler et al. 2012) suggest referring to the (linear) size of the interrogation window l_1 (or interrogation volume I_V in tomographic PIV) instead of the particle tracer displacement. This is justified by the fact that the measurement of spatial resolution is directly connected with the size of the interrogation window, which becomes independent of the pulse separation time when multi-pass interrogation methods are used.

As a result, Eq. (1) can be rewritten as

$$\text{DSR} = \frac{L}{I_V} \quad (2)$$

The above ratio can also be interpreted as the number of independent vectors along a chosen direction within the measurement domain. The minimum size of the interrogation volume in tomographic PIV must comprise 5 to 10 tracers (Scarano 2013). Therefore, the interrogation volume size depends on the average particle concentration C . For a uniform distribution of tracers, the interrogation volume reads as

$$I_V = \sqrt[3]{\frac{N_I}{C}} \quad (3)$$

where N_I represents the particle image number density, defined as the number of particle images per interrogation volume (Keane and Adrian 1990), and C is expressed in number of tracers per unit of volume. Substituting Eq. (3) into Eq. (2) yields

$$\text{DSR} = \frac{L}{I_V} = L \left(\frac{C}{N_I} \right)^{\frac{1}{3}} \quad (4)$$

The size of the measurement domain (L) is typically determined by the geometry of the model under study and the specific flow features of interest. The particle image density is chosen in order to maximize the spatial resolution and the number of particle image pairs for the cross-correlation analysis. As a consequence, the concentration is the parameter most easily varied to achieve the desired DSR. When using HFSB tracers, the concentration is limited by the maximum rate at which they can be released by an emitter. Moreover, given their large size and the limited lifetime (reported to be within 120 s, Bosbach et al. 2009),

the tracers are only used once, since they do not circulate around closed-loop wind tunnels. The present discussion is based on the hypothesis that HFSB tracers are released by an emitter at a rate \dot{N} [bubbles/s] and travel without disturbing the flow within the stream-tube of cross section A corresponding to that of the emitter, with a velocity U . The rate at which the bubbles cross a plane normal to their direction of convection reads as:

$$\dot{N} = CAU \tag{5}$$

A simple example is given here to illustrate the requirements in terms of bubble production rate. Let us assume that a stream-tube with velocity of 10 m/s and a quadratic cross section of $1 \times 1 \text{ m}^2$ is to be seeded at a concentration of 5 bubbles/cm³ ($I_V = 1 \text{ cm}$ for $N_I = 5$). The generation system needs to supply tracers at $\dot{N} = 50 \times 10^6$ bubbles/s, which exceeds by three orders of magnitude the production rate of a single generator. The resulting DSR for such conditions would be around 100, which compares well to that of many planar PIV experiments reported in the literature (Raffel et al. 2007).

Substituting C from the last expression into Eq. (4), the DSR reads now as:

$$DSR = L \left(\frac{\dot{N}}{N_I AU} \right)^{\frac{1}{3}} \cong \left(\frac{L \dot{N}}{N_I U} \right)^{\frac{1}{3}} \tag{6}$$

In the last derivation on the right-hand-side term, it is assumed that $A \approx L^2$, i.e. the seeded stream-tube cross section is comparable to the characteristic length of the object of interest. Equation (6) states the dependence of the DSR upon the characteristic length of the measurement volume, the amount of HFSB entering the measurement volume per unit of time and the local stream velocity.

The bubble rate in the measurement volume \dot{N} is thereby pivotal to achieve the required DSR. High values of \dot{N} yield a high concentration, which in turn increases the dynamic

spatial range. On the other hand, as in every tomographic PIV experiments, the number of ghost particles (Maas et al. 1993) increases rapidly with the density of particle images (Discetti 2013), which affects the accuracy of tomographic reconstruction and motion analysis, as discussed in the work of Elsinga et al. (2011). However, as shown in recent experiment with HFSB (Scarano et al. 2015), the particle image density levels achieved are far below the critical value of 0.05 ppp (particles per pixel) suggested in the work of Elsinga et al. (2006). Finally, the DSR is inversely proportional to the stream velocity U .

Equation (6) can also be interpreted as follows: For a given value of the Reynolds number, higher values of DSR can be achieved increasing the size of the scaled model and reducing the velocity. It may be concluded that scaling up the Reynolds number with the geometrical scale is a more convenient approach than increasing the velocity for achieving a high DSR with HFSB tracers.

The location of the seeding emitter inside the wind tunnel also affects the DSR of the measurement. Here, two relevant cases are discussed. The seeding probe could be installed inside the settling chamber (Fig. 1, left) or downstream the contraction ahead the test section (Fig. 1, right). In the latter case, the emitter must be placed sufficiently far upstream of the measurement volume such that to allow a sufficient decay of its wake. The presence of the contraction changes the flow velocity in which the seeding is released by a factor $1/\rho$, where ρ is defined as the ratio between the cross-sectional area of the injector and that of the seeded stream-tube in the test section.

As a consequence of the different volume of air seeded per unit of time, the concentration of flow tracers depends upon the chosen configuration. Assuming the cross section of the seeding probe to be L_{inj}^2 , with a constant bubble injection rate into the flow \dot{N} , the seeding concentrations read as:

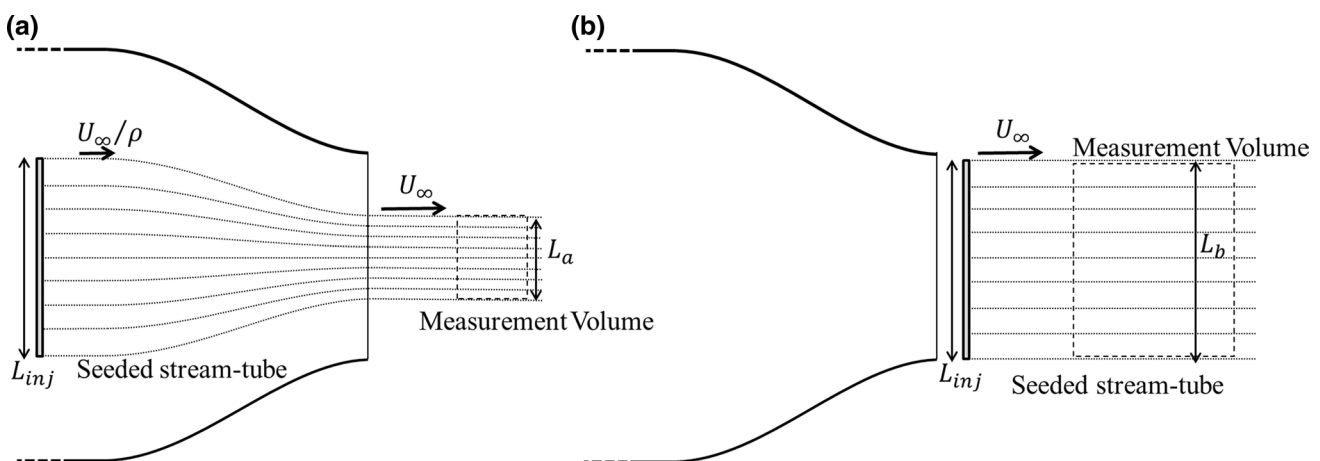


Fig. 1 Sketch of the seeded stream-tube for the injection inside the settling chamber ($\rho > 1$) and downstream the contraction ($\rho = 1$)

$$C = \frac{\dot{N}}{L_{\text{inj}}^2 (U_{\infty}/\rho)} \quad (7)$$

In the above equation, the flow is assumed incompressible and lateral spreading of the stream-tube due to turbulent mixing is neglected. Equation (7) shows that the concentration of HFSB is higher when the emitter is placed in the settling chamber ($\rho > 1$). Conversely, the flow contraction reduces the cross section of the seeded stream-tube scale, which may be regarded as a disadvantage when the measurement region needs to cover large objects. The relationship between the emitter characteristic length and that of the seeded stream-tube is

$$L = \rho^{-1/2} L_{\text{inj}} \quad (8)$$

Combining Eq. (4) with Eqs. (7) and (8), it is possible to retrieve the DSR ratio between the two configurations as follows

$$\frac{\text{DSR}_a}{\text{DSR}_b} = \frac{L_a}{L_b} \left(\frac{C_a}{C_b} \right)^{\frac{1}{3}} = \rho^{-\frac{1}{6}} \quad (9)$$

The ratio expressed in Eq. (9) represents quantitatively the effect of the contraction on the DSR in a tomographic PIV experiment. The dependence upon the 1/6 root indicates that the ratio in Eq. (9) is weakly dependent upon the chosen configuration, however, with a slight advantage in case the emitter is placed directly in the wind tunnel free-stream. Furthermore, in many situations, the access to the settling chamber is limited if not impossible; thus, case *b* remains a more practical choice.

Figure 2 shows the dependence of the HFSB concentration C and the DSR upon the size of the emitter L_{inj} and the seeded stream-tube contraction ρ . The calculation is made assuming free-stream velocity of 8.5 m/s, a bubble emission rate of 8×10^5 bubbles/s and a particle image number

density of 5 (corresponding to the current experiment presented in the remainder). Four values of the contraction ratio ρ are considered, namely 1, 3, 9 and 18, covering a range commonly encountered in low-speed wind tunnels (the last three numbers correspond to the OJF, W-tunnel and LTT wind tunnel, respectively, of the aerodynamics laboratory of TU Delft). The case with unit contraction corresponds to case *b* where the injector is placed in the test section upstream of the model (present experiment). These results are used to predict the concentration and the DSR for a given seeding system.

Increasing the size of the injector is detrimental to the seeding concentration if additional bubble generators are not added into the system. In Fig. 2 (left), for example, the concentration reduces of one order of magnitude when L_{inj} increases from 20 to 100 cm. In contrast, the dynamic spatial range increases with the size of the emitter and of the seeded stream-tube. On the other hand, the dynamic spatial range increases with the size of the seeding injector. In Fig. 2, the working point of the seeding system used in the present experiment (described in the following section) is also shown. The seeding system was used in configuration *b*, with the bubbles injector placed in the test section.

Due to the limited HFSB concentration, typically not exceeding a few bubbles per cubic centimetre, experiments conducted with HFSB are suited for image analysis based on PTV (particle tracking velocimetry) approaches, which requires that the average distance between the particles is large with respect to the average particle displacement (Maas et al. 1993). The equations discussed above remain conceptually valid also for PTV analysis, provided that the image number density is set to unity: $N_I = 1$. It is well known that PTV approaches allow higher spatial resolution, whereas cross-correlation approaches yield higher probability of valid vector detection (Adrian 1991). Furthermore,

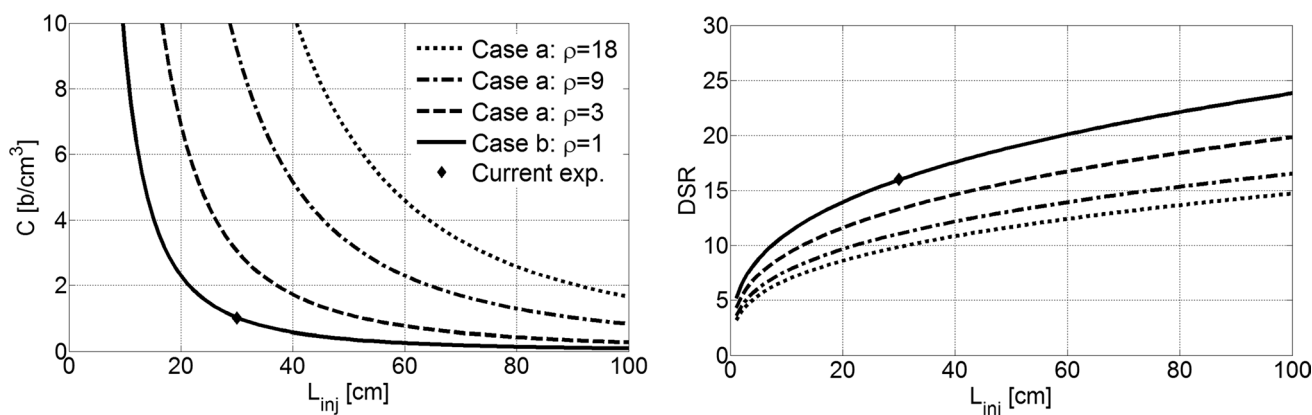


Fig. 2 Concentration (left) and DSR (right) as function of the characteristic length of the injector and of the contraction ratio. Equation (7) is used to retrieve C . DSR was computed using Eq. (6) where L is replaced by the relation expressed in Eq. (8) ($\dot{N} = 8 \times 10^6$, $U_{\infty} = 8.5$ m/s)

Table 1 Dynamic spatial range for relevant Tomographic PIV experiments in air flows

Work in the literature	Measurement domain linear size L [mm]	Interrogation box linear size I_B [mm]	DSR
Elsinga et al. (2006)	40	2.1	19
Staack et al. (2010)	50	2.5	20
Schröder et al. (2011)	63	2.7	22
Kühn et al. (2012) ^{a,b}	840	38	22
Fukuchi (2012)	160	5	30
Scarano et al. (2015) ^a	200	20	10
Current study ^a	400	33	13

^a Experiment conducted with HFSB

^b Experiment conducted in a closed volume

correlation-based techniques yield velocity data defined in a regular Cartesian grid, which is better suited for the computation of spatial derivatives and flow-derived properties as vorticity.

A survey of tomographic PIV experiments is given in Table 1 where the achieved DSR is reported. The dynamic spatial range of tomographic PIV experiments typically varies between 20 and 30. The recent introduction of HFSB certainly increases the measurement domain size, at the cost, however, of a lower DSR, mostly ascribed to the poor concentration of the tracers. The latter limitation is partly due to the current unavailability of HFSB generators that can accurately produce neutrally buoyant tracers at rates in the order of 10^7 – 10^8 bubbles/s. Moreover, the less fundamental, yet very relevant problem of uniformly introducing the tracers upstream of the test section with minimum intrusion to the free-stream flow conditions requires dedicated technical solutions. The remainder of this study describes the concept and the realization of a seeding system that multiplies the instantaneous bubble emission rate from a single generator to produce a quasi-uniform stream of seeded flow in a large-scale wind tunnel.

3 Seeding system

The HFSB generator used in the present experiment was provided by LaVision GmbH, and it is based on a design made by the German Aerospace Centre (DLR). The working principle is described in the work of Bosbach et al. (2009). The present bubble generator has the highest production rate, 50,000 bubbles/s, among other devices reported in the literature (Okuno et al. 1993; Müller et al. 2001; <http://www.sageaction.com/>), as shown in Table 2. In the previous work of the authors (Scarano et al. 2015), such bubble generator was placed downstream the contraction and was able to generate a seeded stream-tube of 3 cm width with no noticeable variation for a range of

Table 2 Production rate of different HFSB generators

Research group	Production rate [bubbles/s]
Toyota—Tokyo University	3000
Sage Action Inc.	300–400
RWTH Aachen University	500
DLR	50,000

free-stream velocity between 1 and 30 m/s. It can be concluded that the use of a single generator is deemed unsuited for conducting large-scale tomographic PIV experiments.

The approach followed to increase both the rate of tracers injected in the flow as well as the size of the seeded stream-tube makes use of a dedicated system (Fig. 3) composed of a HFSB generator that releases the bubbles inside of a large cylindrical reservoir (30 cm diameter, approximately 70 L volume). The HFSB tracers are temporarily accumulated, while a piston driven by an electrical linear actuator increases the available volume. At the end of the expansion, the piston rapidly inverts its motion and conveys the air and the bubbles from the reservoir towards an injector placed in the wind tunnel through a flexible pipeline (3.6 cm diameter and 1.7 m length). The latter is connected to the injector that distributes the tracers within a stream-tube.

The aerodynamic rake can be placed in the settling chamber of the wind tunnel as done in the experiments reported in the previous work of the authors (Scarano et al. 2015), or directly placed in the free-stream as done in the current experiments. In the latter case, as discussed in Sect. 2, the expected cross section of the stream-tube coincides with that of the seeder. The geometry of the injector is presented in Fig. 4 and consists of an aerodynamic rake with 12 bi-convex airfoils, with a chord of 10 cm and a thickness of 1.2 cm, arranged over two staggered rows. Each airfoil has 22 orifices with a diameter of 3 mm along the trailing edge. The overall cross section of the rake is

Fig. 3 *Left* schematic description of seeding storage and transient injection system. *Right* photograph of aerodynamic rake

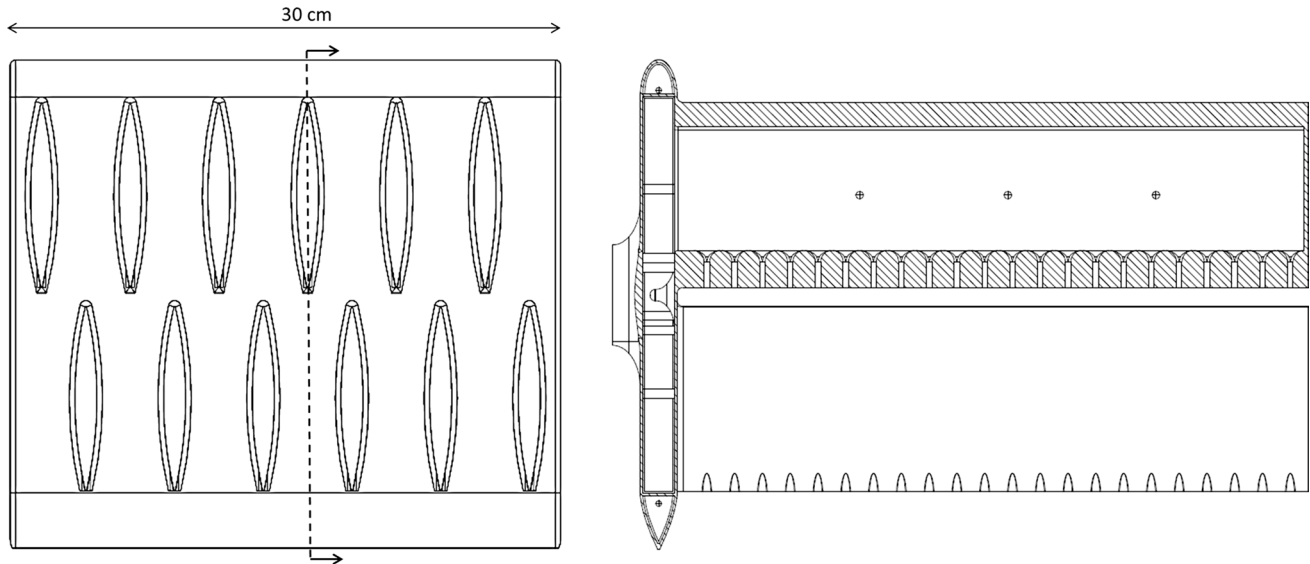
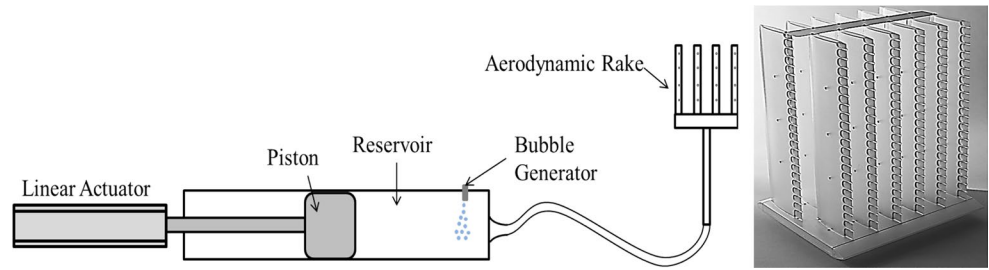


Fig. 4 Scale drawing of aerodynamic rake with 12 bi-convex airfoils staggered in two rows and with 264 orifices. *Left* top view; *right* section view

$30 \times 36 \text{ cm}^2$; only 550 cm^2 are obstructed by the airfoils and therefore contribute to the blockage (considering the total amount of 12 airfoils). However, one should keep in mind that the airfoils are placed in two rows of six, which are staggered with respect to each other, thus reducing the blockage. This is considered negligible, $<6\%$ blockage, in large wind tunnels with cross section of 1 m^2 or larger. Finally, the air flow injected with the HFSB from the seeding probe depends on the stroke of the piston and the injection time. In the present work, the additional air flow rate was $0.04 \text{ m}^3/\text{s}$. The latter is rather small in comparison with the air flow crossing the overall cross section of the rake at 10 m/s (approximately $1 \text{ m}^3/\text{s}$), and it is certainly negligible when compared to the wind tunnel air flow rate.

The production rate of the bubble generator installed in the reservoir is indicated with \dot{N}_0 . In the present case, $\dot{N}_0 = 50,000$. The piston moves backward at constant speed, increasing the available volume during a time interval Δt_0 (accumulation time). After that, the piston rapidly moves forward during a time interval Δt_1 (release time). The total number of bubbles produced during one period of

the piston motion is $\dot{N}_0(\Delta t_0 + \Delta t_1)$. In the ideal case where all the produced bubbles are ejected from the system during release, the rate at which the bubbles exit the cylindrical reservoir in Δt_1 is \dot{N}_1 :

$$\dot{N}_1 = \dot{N}_0 \frac{\Delta t_0 + \Delta t_1}{\Delta t_1} \approx \frac{\Delta t_0}{\Delta t_1} \dot{N}_0 = G \dot{N}_0 \tag{10}$$

The accumulation time needs to be shorter than the lifetime of the bubbles (2 min). In the present case, $\Delta t_0 \gg \Delta t_1$. The time ratio $\Delta t_0/\Delta t_1$ represents the gain factor G of bubble rate obtained by the seeding system compared to a single bubble generator. Assuming that during the accumulation phase, all the bubbles stay in the cylindrical reservoir, whose maximum volume during the accumulation time Δt_0 is V_0 , and the bubbles concentration within the reservoir is:

$$C_0 = \frac{\dot{N}_0 \Delta t_0}{V_0} \tag{11}$$

Outside of the seeding system, the bubbles concentration decreases to C due to dilution with the air flow crossing the injector during release:

$$C = \frac{\dot{N}_1 \Delta t_1}{V_0 + V_{wt}} = \frac{\dot{N}_0 \Delta t_0}{V_0 + V_{wt}} \tag{12}$$

V_{wt} is the air volume flowing through the diffuser and in which the bubbles are ejected. The term V_{wt} can be expressed as:

$$V_{wt} = Au\Delta t_1 \tag{13}$$

where u is the velocity of the flow in which the HFSB are injected and is equal to U_∞/ρ in case *a* (injector in the settling chamber) and U_∞ in case *b* (injector in the test section; see Sect. 2). Substituting Eq. (13) into Eq. (12) and making use of the definition of the gain factor, the expression of the concentration becomes:

$$C = \frac{\dot{N}_0 G}{\frac{V_0 + V_{wt}}{\Delta t_1}} = \frac{\dot{N}_0 G}{\frac{V_0}{\Delta t_1} + Au_\infty} = \frac{\dot{N}_0 G}{\dot{V}_0 + Au_\infty} \tag{14}$$

Equation (14) shows the dependence of the concentration from the main working parameters of the seeding system. The choice of the bubble generator determines the bubbles production rate, \dot{N}_0 , and therefore is crucial for the optimization of C . The latter is directly dependent upon the gain factor, which is varied by changing the accumulation time Δt_0 , provided it does not exceed the bubbles lifetime. The cross section of the seeded stream-tube A , determines the air volume flow rate where the bubbles are released and therefore the dilution in the wind tunnel. Increasing A reduces the concentration of tracers.

Using Eq. (14) with the values in Table 3, corresponding to the experiment described in the next section, a theoretical concentration (C_{th}) of 3 bubbles/cm³ is expected. This concentration allows tomographic PIV measurements to investigate flow structures of the order of a few centimetres, as it will be done in the next section for the analysis of the blade tip vortex of a vertical axis wind turbine. The concentration observed within the measurements (C_{meas}) is considerably less than the above one (1 bubble/cm³) as shown in Fig. 2, left. This difference is ascribed to a number of factors, most importantly, bubbles extinction during their transport from the reservoir to the exit of the injector and bubble collisions inside the reservoir. As a result of the lower concentration, the tomographic PIV analysis

is conducted with larger interrogation windows, yielding in turn a lower spatial resolution.

Concluding, it was noticed that the loss of bubbles upstream of the injector poses some limits to the seeding system described above. A possible solution to comply with this issue will be the use of many bubble generators in parallel installed inside the wind tunnel. A multi-generator system allows producing HFSB directly in the stream of the wind tunnel without transport losses and introduction of the air volume V_0 . The latter alternative, however, requires a large number of nozzles, on the order of G for a given $\dot{N}_0 = 50,000$ in order to retrieve the same concentration and DSR obtained for the present seeding system. Although a multi-generator system is not yet available at present time, the analysis performed in the present section can be extended to the latter case, provided that a unitary gain factor ($G = 1$) and the total production rate of all nozzles are considered.

4 Wind tunnel experiment

The above described system is used to perform time-resolved tomographic PIV measurements on a scaled model of vertical axis wind turbine (VAWT). The measurements are taken in the Open Jet Facility (OJF) of TU Delft. The wind tunnel features an open test section with closed-circuit. At the end of the contraction, the wind tunnel has an octagonal cross section of 2.85×2.85 m². The air flow is driven by a 500 kW electric motor. In the test section, the free-stream velocity can range from 3 to 35 m/s with a maximum turbulence intensity of 0.5%. The model is a two-blade H-shaped rotor VAWT of 1 m diameter (D). The rotor blades are shaped following the NACA0018 profile with 6 cm chord length and installed with zero angle of attack. The blades are tripped by zig-zag stripes in order to force the boundary layer transition from laminar to turbulent regime and avoid the occurrence of laminar separation bubbles. The blade span H is 1 m long, yielding an aspect ratio $AR = H/D = 1$. Measurements are taken at free-stream velocity $U_\infty = 8.5$ m/s and rotational speed $\Omega = 800$ rpm, yielding a tip speed ratio $\lambda = 5$. The Reynolds number based on the chord length and the tangential velocity of the blades is $Re_c = 170,000$.

Table 3 Theoretical and measured bubble concentration for the VAWT experiment

\dot{N}_0 (b/s)	Δt_0 (s)	Δt_1 (s)	G	V_0 (cm ³)	A (cm ²)	U_∞ (m/s)
50,000	50	1	50	16,000	900	8.5
C_{th} (b/cm ³)		C_{meas} (b/cm ³)			DSR _{th}	DSR _{meas}
3		1			28	13

The choice of the frame of reference and associated terminology follow the work of Tescione et al. (2014). The schematic from the latter authors is shown in Fig. 5. The Cartesian coordinate system has its origin at the bottom surface of the blade and azimuthal angle $\theta = 0^\circ$ (windward position). The free-stream velocity is directed along x . The turbine rotates clockwise when seen from the top.

Figure 6 illustrates the arrangement of the seeding system and tomographic setup in the wind tunnel. The

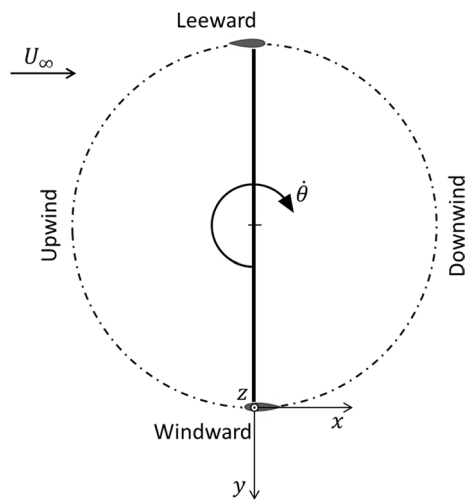


Fig. 5 System of reference and schematic of the blade motion on a vertical axis turbine

cylindrical reservoir is placed below the wind tunnel exit; the seeding injector was installed at the exit of the wind tunnel 2.5 m upstream of the VAWT model. A stream-tube of tracers is released such that it flows around the bottom tip of the blade when it is at $\theta = 0^\circ$.

The turbulence intensity of the stream before it interacts with the wind turbine is assessed by dedicated measurements returning rms fluctuations below 2% of the free-stream. The HFSBs injected in the flow have an average diameter of approximately 300 μm . The bubbles are generated in the same condition as it is described in the work of Scarano et al. (2015) and have a characteristic response time in the order of 10 μs .

The tomographic PIV system consists of a Quantronix *Darwin Duo* Nd:YLF laser (2×25 mJ at 1 kHz) and three Photron Fast CAM SA1 cameras (CMOS, 1024×1024 pixels, 12-bit and pixel pitch 20 μm). The optical magnification is approximately $M = 0.05$, and the extent of the measured domain is $40 \times 20 \times 15$ cm^3 . The lens aperture is set to $f/11$ to ensure images in focus over the entire depth. Under these conditions, images are recorded with a particle density of approximately 0.004 ppp (4000 particles/Mpixel) and the typical particle peak intensity is 300 counts.

Image acquisition and processing is performed using the LaVision software *DaVis 8.2.2*. Image pre-processing consists of image background elimination via minimum subtraction and Gaussian filter (3×3 pixels). The domain is

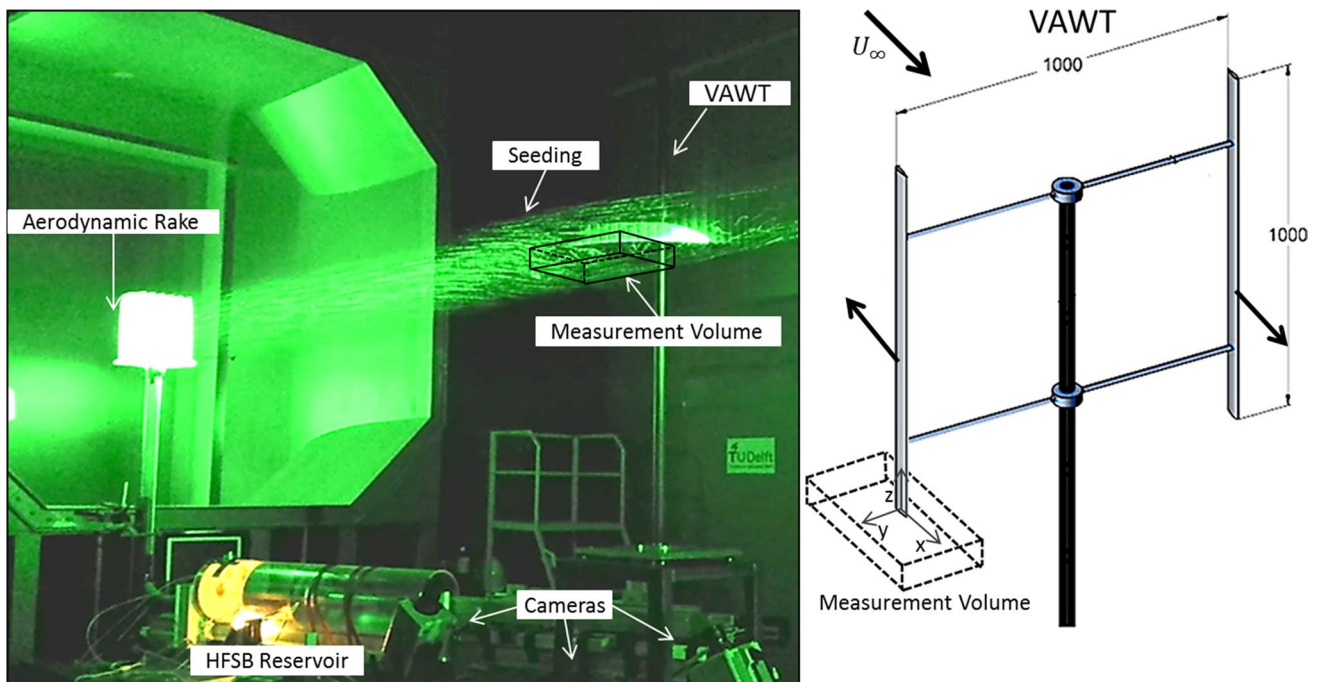
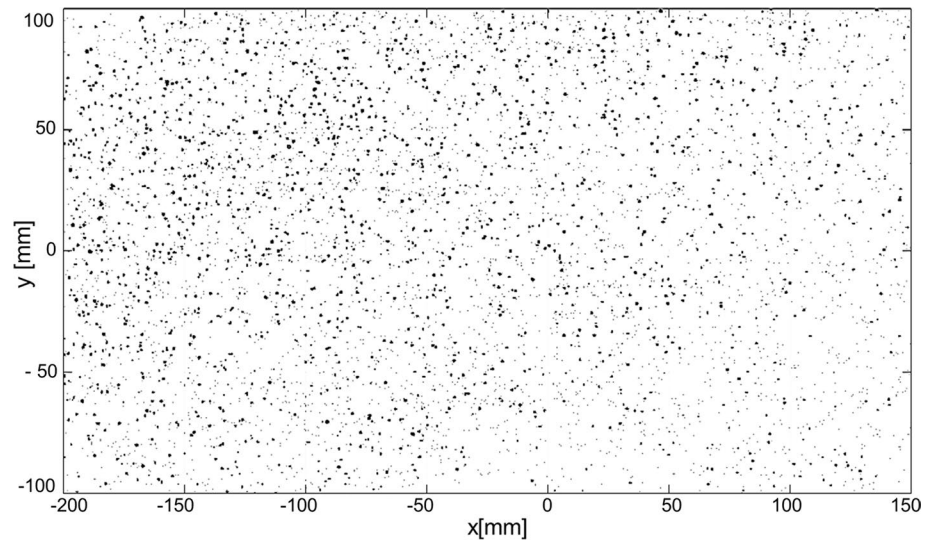


Fig. 6 Arrangement of the experimental set-up, with the HFSB released by the aerodynamic rake installed at the exit of the wind tunnel. Cylindrical reservoir, cameras and indication of the measured volume (left). Sketch of the VAWT with dimensions in millimetres (right)

Fig. 7 Raw image from camera 2 (inverted grey levels)



discretized into $910 \times 814 \times 456$ voxels and reconstructed with 10 iterations of the fast MART algorithm. The objects are interrogated with correlation blocks of $80 \times 80 \times 80$ voxels ($3.3 \times 3.3 \times 3.3 \text{ cm}^3$) and 75% overlap factor, yielding $42 \times 35 \times 23$ vectors with a grid spacing of approximately 8 mm. The resulting vector fields are post-processed with the universal outlier detection algorithm (Westerweel and Scarano 2005).

Moreover, Tomo-PTV analysis is performed on the same recordings in the vortex region to evaluate the effects of spatial resolution on the estimates of peak vorticity and vortex core diameter. The method is based on the Vortex-in-Cell (VIC) technique, introduced by Schneiders et al. (2014), and it is used in the analysis of the peak vorticity for comparison with the cross-correlation-based results. The method is used to reconstruct velocity fields on a regular grid from volumetric particle-tracking measurements. The time-resolved reconstructions, used for the tomographic PIV, are also used for a tomographic PTV analysis. The locations of the particles are identified with sub-voxel accuracy using a 3-point Gaussian fit. The 3D trajectories allow the determination of the velocity and acceleration through a second-order polynomial fit along seven snapshots. The dense interpolation of the velocity from the sparse PTV-grid onto a regular one is made using an iterative minimization problem of a cost function that is proportional to the difference between the PTV measurements and the VIC+ results. The minimization is constrained by the incompressible flow assumption and the momentum equation in vorticity–velocity formulation. Due to their different dimensions, velocity and acceleration are scaled in the cost function by a factor α , which is chosen to be equal to the ratio of the typical magnitude of velocity and acceleration calculated from

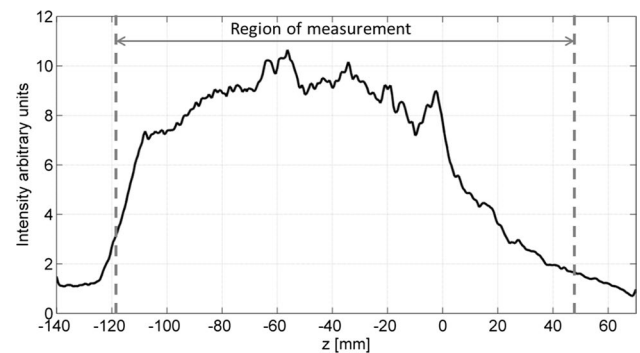


Fig. 8 Span-wise profile of reconstructed light intensity

their root-mean-squared value. The VIC+ step is initialized using a uniform flow in the free-stream direction. The computational domain is chosen 30% larger than the measurement volume with constant boundary conditions based on the free-stream. The mesh spacing equals to 20 voxels. After the computation, the volume is cropped to the measurement volume and the exterior is not considered for data analysis. For full details of the VIC+ method, the reader is referred to Schneiders and Scarano (2016).

The recordings are acquired at 1 kHz, resulting into time-resolved information for the particle-tracking technique. Figure 7 shows the particle image density for a typical recording.

The quality of tomographic calibration and reconstruction is verified inspecting the reconstructed light intensity distribution along the volume depth (Fig. 8). The profile, obtained from the average over 400 instantaneous objects, yields a reconstruction signal-to-noise ratio (Lynch and Scarano 2014) above 7 in most of the domain.

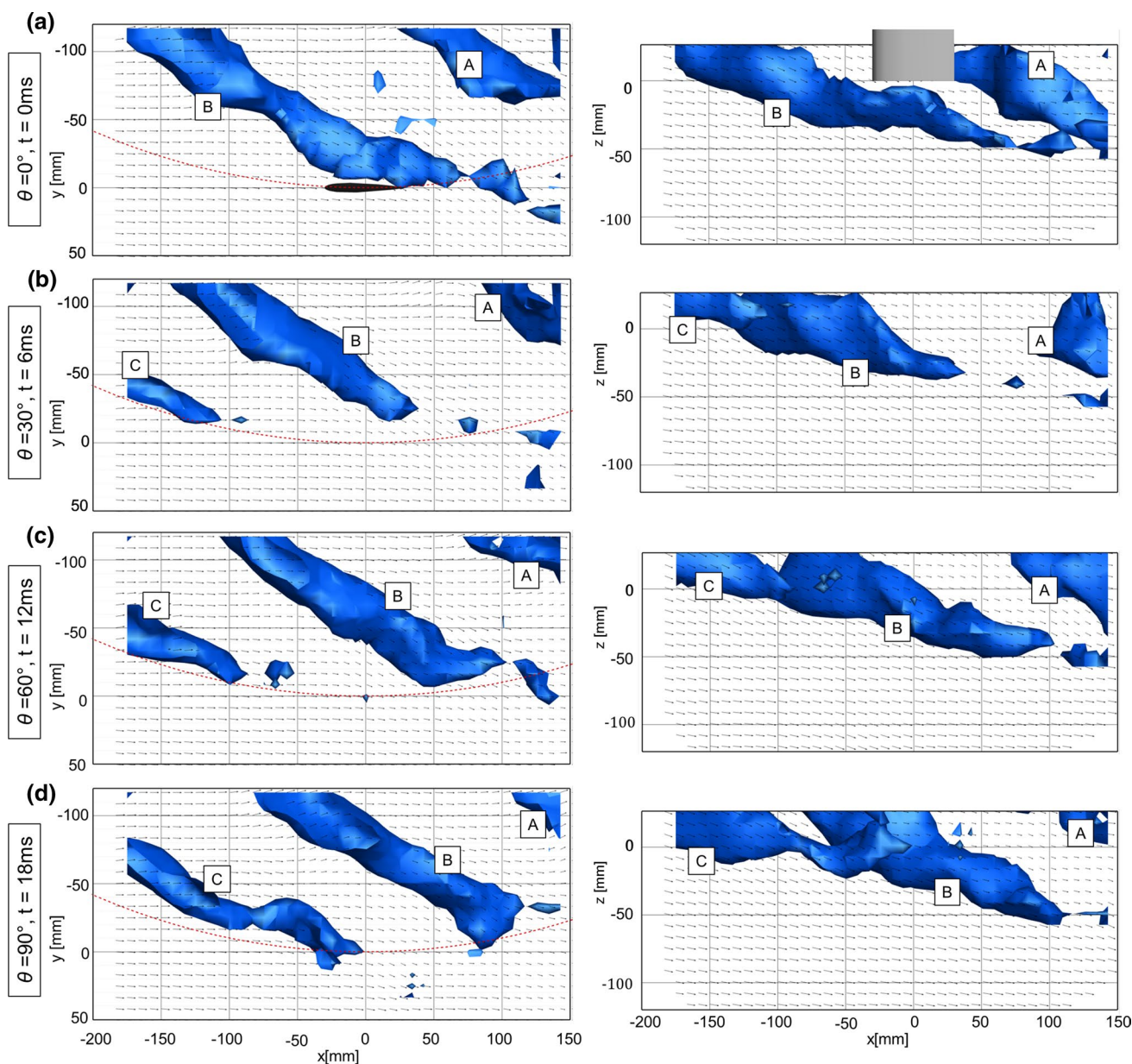


Fig. 9 Instantaneous velocity vector field (from cross-correlation) and vorticity magnitude iso-surface ($\omega = 170/s$) for tip vortices generated by the retrograding blade in a VAWT. One plane of velocity

vectors represented at $Z = 0$ (left) and at $Y = -50$ mm (right). Red dashed line represents the blade trajectory

4.1 Results

The temporal evolution of the tip vortices emanating from the blade tip is illustrated by a sequence of four instantaneous velocity and vorticity fields (Fig. 9) at angular positions of the blade: $\theta = \{0^\circ, 30^\circ, 60^\circ, 90^\circ\}$, corresponding to time steps of 6 ms. The vorticity was computed with an approximation of a grid point with a second-order central scheme. A more detailed representation is given with the animation Movie 1. In Fig. 9, the column on the left shows the top view of the measured velocity and vorticity field, while the right

column gives the lateral view. The large-scale tomographic PIV returns the presence of tip vortices regularly generated by the motion of the retrograding blade from the windward to the upwind position. A portion of the blade is captured inside the measurement volume only for $\theta = 0^\circ$ shown in Fig. 9a. When the blade is at $\theta = 0^\circ$, it passes through the condition of zero incidence, where no lift is generated. At this particular location, the blade is not releasing any tip vortex; therefore, the vortical structures present in the measurement domain, indicated as A and B in Fig. 9a, have been released by prior blade passages and convected downstream.

When the blade is in position $\theta = 30^\circ$, it releases a tip vortex of finite and measurable strength, labelled with C in Fig. 9b. The vortices A, B and C are convected downstream by the flow field and their mutual distance depends on the tip speed ratio. From the side views of Fig. 9, it is clear that the vortical structures also convect outboard (towards negative values of Z), departing downward from the blade tip plane ($Z = 0$). The tip vortex C released by the blade at $\theta = 30^\circ$ (Fig. 9b) appears weaker than the vortex generated with the blade at higher angle of attack (Fig. 9c, d). The change in the vortex strength is related to the variation of the lift generated as the blades rotate. The observed behaviour agrees with the three-dimensional unsteady RANS simulation of Howell et al. (2010), where strong correlation between the maximum developed lift and maximum strength of the tip vortex was documented.

The span-wise velocity profile along the vertical direction of the tip vortex B (Fig. 9b) is shown in Fig. 10. The position of the core is determined using the peak value of vorticity. The profile is extracted at plane $X = 50$ mm for 10 successive blade passages at $\theta = 30^\circ$. The tip of the blade is located at $Z = 0$, the negative values correspond to the outboard region. The instantaneous profiles show pronounced velocity fluctuations inside the rotor region ($Z > 0$), whereas the outboard region exhibits a more stable behaviour. The

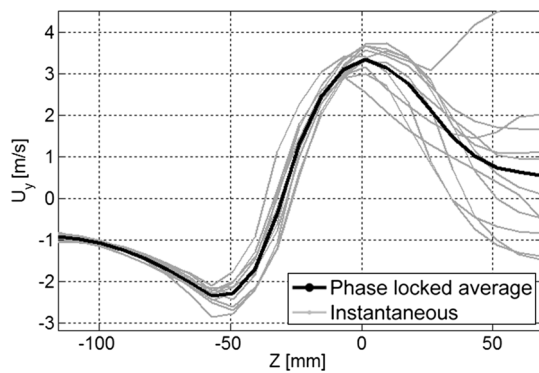


Fig. 10 Vertical profile of span-wise velocity component of the tip vortex B across the location of the vorticity ($X = 50$ mm, $\theta = 30^\circ$)

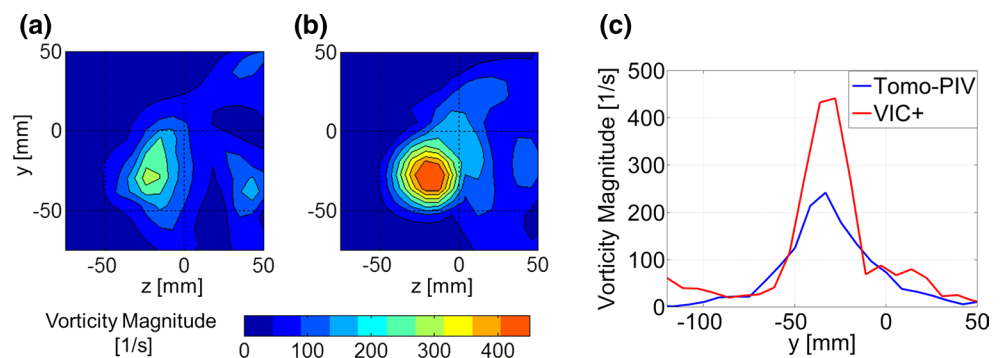
variations of the velocity profiles are therefore localized in the turbulent wake of the blades, in which the laminar–turbulent transition of the boundary layer is forced with the tripping procedure. In addition, the wakes generated by the blades in the upwind position ($0^\circ < \theta < 180^\circ$) are transported downstream through the inner region of the rotor. As a result, the velocity field is characterized by higher fluctuations at this location, as reported by the experimental results of Tescione et al. (2014). The interaction between the blades and their own wakes, produced in the previous rotation, influences the flow condition in the pressure and suction sides with a consequent effect on the generation and development of the tip vortices.

Figure 11 shows a comparison of the two techniques on an instantaneous vorticity contour of vortex B extracted at $X = 0$ mm. The VIC+ result exhibits a peak vorticity approximately two times higher than that returned with cross-correlation. These discrepancies are ascribed to the higher spatial resolution of the PTV-based algorithm.

Similarly to the analysis made on aircraft wing-tip vortices (Scarano et al. 2002), limited spatial resolution causes peak modulation and vortex diameter overestimation; their combined effect is less detrimental in terms of vortex total circulation, which relates to the integral of vorticity. In Fig. 11, a clear difference of the vortex diameter is not evident. Therefore, the circulation associated with the vortex is expected to be underestimated when measured with tomographic cross-correlation compared to VIC+.

The peak values of vorticity presented in the work of Tescione et al. (2014) are also approximately 300 1/s, but the value only pertains to the y -component as obtained from planar and stereoscopic PIV measurements. The three-dimensional structure of the vortices shed from VAWT would require rotating the measurement angle with the blade position to compensate from the rotation of the vorticity vector. For practical reasons, experiments are often conducted at a fixed orientation of the measurement plane that only provides one component of the vorticity vector (not generally aligned with the axis of the vortex). Large-scale tomographic PIV allows the measurement of the three components of the vorticity vector, enabling the

Fig. 11 Comparison between cross-correlation and VIC+ for the instantaneous vorticity magnitude of the tip vortex B (Fig. 9a). Vorticity magnitude colour contours with cross-correlation (a) and VIC+ (b). Vertical profiles of the vorticity (c)



three-dimensional inspection of the vortex structure, which is strongly affected by the characteristic flow curvature in the rotor region of VAWT. However, as shown in the current experiments, the limited spatial resolution of this approach poses a caveat on the interpretation of peak vorticity and circulation (Fig. 11c).

Figure 11 shows the axial distribution of peak vorticity in vortex B, as shown in Fig. 9a. The peak vorticity is presented along the stream-wise direction X , approximately corresponding to the direction of the vortex axis. The distribution corresponds to the angular position $\theta = 0^\circ$ of the blade. The instantaneous measurements (thin lines) are presented along with the corresponding phase average (thick line). The peak vorticity decreases monotonically moving downstream, which is consistent with the increase in lift generated by the blade when it rotates from $\theta = 0^\circ$ to higher values of the phase angle. The results obtained by cross-correlation analysis are significantly below the estimates returned with VIC+, which has also been reported in a study by Schneiders et al. (2016). This is mainly due to the more pronounced effect of spatial filtering associated with the cross-correlation operator. Despite the aforementioned effect, the cross-correlation analysis returns a consistent characterization of the tip-vortex topology, the induced velocity field and the dynamical evolution of the vortex.

The instantaneous data exhibit a significant dispersion around the phase-average value (Fig. 12). The latter cannot be explained by the effect of measurement noise as the flow exhibits turbulent behaviour mainly ascribed to the wake of the blade in the inner rotor region of the VAWT. In the vorticity field retrieved with VIC+, additional rib-like vortical structures are observed that connect two consecutive tip vortices while convecting downstream (black arrows pointing at them in Fig. 13). These interactions do not exhibit as regular occurrence as encountered in shear layers dominated by Kelvin–Helmholtz vortices (Lopez and Bulbeck

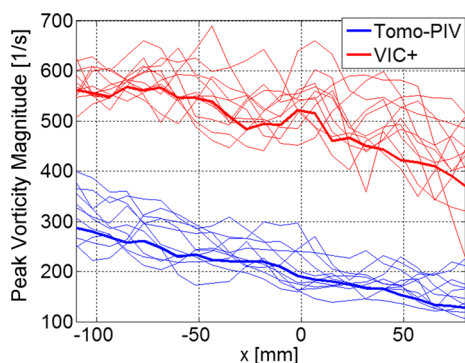


Fig. 12 Peak vorticity magnitude of the tip vortex B (Fig. 9) with the blade at position $\theta = 0^\circ$. *Thin lines* correspond to instantaneous measurements and *thick lines* to the phase average

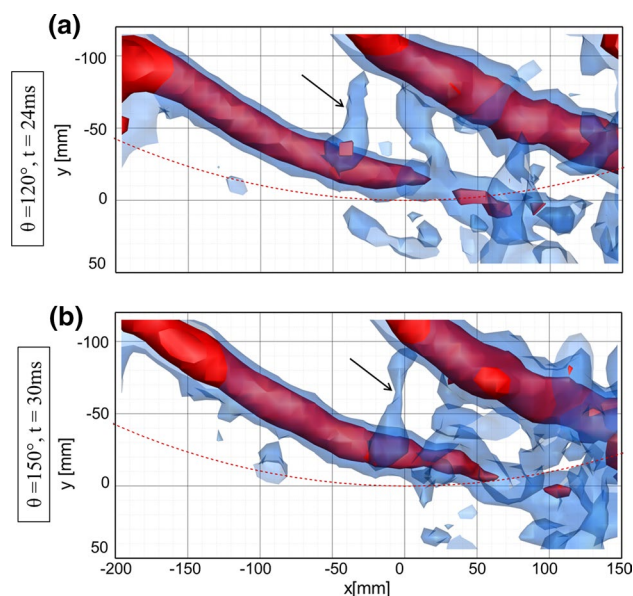


Fig. 13 Instantaneous iso-surfaces of vorticity magnitude (*red*: 300/s, *blue*: 170/s) returned by VIC+ data processing

1993), however, their structure resembles that of rib-like vortices interconnecting co-rotating tip vortices. The intensity of such ribs has lower values of vorticity compared with those of the tip vortices ($|\omega| < 200$ 1/s), and they are expected to contribute in destabilizing the tip vortices during their dynamical evolution in the rotor wake region.

5 Conclusions

In the present study, the relationship between the measurement of DSR and the production rate of tracer particles has been derived for the case of HFSB tracers. A dedicated seeding system has been designed to increase the amount of HFSB injected into the flow to overcome the limited production rate of bubble generators for large-scale measurements. The importance of the location where the tracers are injected has been addressed, and the effects on concentration and DSR have been quantified.

The system has been demonstrated by large-scale tomographic PIV measurements for the investigation of the blade tip vortex of a vertical axis wind turbine. Time-resolved measurements in a volume of $40 \times 20 \times 15$ cm³ were taken with a seeding concentration of about 1 bubble/cm³. Data analysis by tomographic PIV describes the flow structure in the rotor region of the VAWT, dominated by large-scale vortices shed from the blade tip. The behaviour of the latter vortex has been described in the near-wake region and its properties examined, in terms of peak vorticity. The comparison of the results from tomographic PIV with a higher resolution PTV analysis based on VIC+

poses a caveat on the quantitative underestimation of peak vorticity, when cross-correlation analysis is used for tomographic PIV at the present level of seeding concentration.

Acknowledgements The authors wish to thank Jan F. G. Schneiders for the contribution in the analysis of the tomographic data with the VIC+ technique.

Open Access This article is distributed under the terms of the Creative Commons Attribution 4.0 International License (<http://creativecommons.org/licenses/by/4.0/>), which permits unrestricted use, distribution, and reproduction in any medium, provided you give appropriate credit to the original author(s) and the source, provide a link to the Creative Commons license, and indicate if changes were made.

References

- Adrian RJ (1991) Particle-imaging techniques for experimental fluid mechanics. *Annu Rev Fluid Mech* 23:261–304
- Adrian RJ (1997) Dynamic ranges of velocity and spatial resolution of particle image velocimetry. *Meas Sci Technol* 8:1393
- Astarita T (2009) Adaptive space resolution for PIV. *Exp Fluids* 46:1115–1123
- Babie BM, Nelson RC (2010) An experimental investigation of bending wave instability modes in a generic four-vortex wake. *Phys Fluids* 22:077101
- Bosbach J, Kühn M, Wagner C (2009) Large scale particle image velocimetry with helium filled soap bubbles. *Exp Fluids* 46:539–547
- Discetti S (2013) Tomographic particle image velocimetry—developments and applications to turbulent flows. Ph.D. thesis
- Elsinga GE, Scarano F, Wieneke B, Van Oudheusden BW (2006) Tomographic particle image velocimetry. *Exp Fluids* 41:933–947
- Elsinga GE, Westerweel J, Scarano F, Novara M (2011) On the velocity of ghost particles and the bias errors in tomographic-PIV. *Exp Fluids* 50:825–838
- Ferrell GB, Aoki K, Lilley DG (1985) Flow visualization of lateral jet injection into swirling crossflow. *AIAA Paper* 85, pp 14–17
- Fukuchi Y (2012) Influence of number of cameras and preprocessing for thick volume tomographic PIV. In: 16th international symposium on applications of laser techniques to fluid mechanics. Lisbon
- Hale RW, Tan P, Ordway DE (1971a) Experimental investigation of several neutrally-buoyant bubble generators for aerodynamic flow visualization. *Naval Res Rev* 24:19–24
- Hale RW, Tan P, Stowell RC, Ordway DE (1971b) Development of an integrated system for flow visualization in air using neutrally-buoyant bubbles. SAI-RR 7107 Sage Action Inc., Ithaca, NY
- Howell R, Qin N, Edwards J, Durrani N (2010) Wind tunnel and numerical study of a small vertical axis wind turbine. *Renew Energy* 35:12–422
- Kähler CJ, Scharnowski S, Cierpka C (2012) On the resolution limit of digital particle image velocimetry. *Exp Fluids* 52:1629–1639
- Keane RD, Adrian RJ (1990) Optimization of particle image velocimeters. Part I: double pulsed systems. *Meas Sci Technol* 1:1202–1215
- Klimas P (1973) Helium bubble survey of an opening parachute flow-field. *J Aircraft* 10:5670–5694
- Kühn M, Ehrenfried K, Bosbach J, Wagner C (2012) Large-scale tomographic PIV in forced and mixed convection using a parallel SMART version. *Exp Fluids* 53:91–103
- Lopez JM, Bulbeck CJ (1993) Behavior of streamwise rib vortices in a three-dimensional mixing layer. *Phys Fluids A* 5:1694–1702
- Lynch KP, Scarano F (2014) Experimental determination of tomographic PIV accuracy by a 12-camera system. *Meas Sci Technol* 25:084003
- Maas HG, Gruen A, Papantoniou D (1993) Particle tracking velocimetry in three-dimensional flows. *Exp Fluids* 15:133–146
- Melling A (1997) Tracer particles and seeding for particle image velocimetry. *Meas Sci Technol* 8:1406
- Müller D, Müller B, Renz U (2001) Three-dimensional particle-streak tracking (PST) velocity measurements of a heat exchanger inlet flow. *Exp Fluids* 30:645–656
- Okuno Y, Fukuda T, Miwate Y, Kobayashi T (1993) Development of three dimensional air flow measuring method using soap bubbles. *JSAE Rev* 14:50–55
- Pounder E (1956) Parachute inflation process wind-tunnel study. WADC Technical Report 56-391, Equipment Laboratory of Wright-Patterson Air Force Base. Ohio, pp 17–18
- Raffel M, Willert CE, Wereley ST, Kompenhans J (2007) Particle image velocimetry—a practical guide, 2nd edn. Springer, Berlin
- Scarano F (2013) Tomographic PIV: principles and practice. *Meas Sci Technol* 24:012001
- Scarano F, van Wijk C, Veldhuis L (2002) Traversing field of view and AR-PIV for mid-field wake vortex investigation in a towing tank. *Exp Fluids* 33:950–961
- Scarano F, Ghaemi S, Caridi GCA, Bosbach J, Dierksheide U, Sciacchitano A (2015) On the use of helium-filled soap bubbles for large-scale tomographic PIV in wind tunnel experiments. *Exp Fluids* 56:1–12
- Schneiders JF, Scarano F (2016) Dense velocity reconstruction from tomographic PIV with material derivatives. *Exp Fluids* 57:139
- Schneiders JFG, Dwight RP, Scarano F (2014) Time-supersampling of 3D-PIV measurements with vortex-in-cell simulation. *Exp Fluids* 55:1692
- Schneiders JF, Scarano F, Elsinga GE (2016) On the resolved scales in a turbulent boundary layer by tomographic PIV and PTV aided by VIC. In: 18th international symposium on the application of laser techniques to fluid mechanics. Lisbon
- Schröder A, Geisler R, Staack K, Elsinga GE, Scarano F, Wieneke B, Westerweel J (2011) Eulerian and Lagrangian views of a turbulent boundary layer flow using time-resolved tomographic PIV. *Exp Fluids* 50:1071–1091
- Staack K, Geisler R, Schröder A, Michaelis D (2010) 3D-3C-coherent structure measurements in a free turbulent jet. In: 15th international symposium on applications of laser techniques to fluid mechanics. Lisbon
- Tescione G, Ragni D, He C, Ferreira CS, van Bussel GJW (2014) Near wake flow analysis of a vertical axis wind turbine by stereoscopic particle image velocimetry. *Renew Energy* 70:47–61
- Westerweel J, Scarano F (2005a) Universal outlier detection for PIV data. *Exp Fluids* 39:1096–1100
- Westerweel J, Elsinga GE, Adrian RJ (2013) Particle image velocimetry for complex and turbulent flows. *Annu Rev Fluid Mech* 45:409–436
- Westerweel J, Scarano F (2005b) Universal outlier detection for PIV data. *Exp Fluids* 39:1096–1100